1 INTRODUCTION

The study of flows in complex geometries is a difficult task that usually requires specialized treatment including body-fitted grid generation. The purpose of this paper is to introduce a flexible method for treating flows past simple shape bodies. Flow past a stationary or moving bluff body can be considered as an extreme case of the interaction between two continuum phases, in which one phase is rigid. The case of a fluid phase interacting with a deformable elastic phase has been treated by the immersed boundary IB method developed by Peskin [1], motivated by the problem of flow in the heart. The case of two immiscible fluid phases separated by an evolving interface has been treated by the volume of fluid VOF method, developed by Hirt and Nichols [2] for the dynamics of free boundaries. The IB method allows one to simulate elastic materials interacting with a fluid where the boundaries are model as pure force-generators. It involves solving the Navier-Stokes equation in Eulerian form for the fluid motion, a fiber force density in Lagrangian form for the material and fiber-fluid interaction equations. The VOF [2], [3], [4] method is an Eulerian scheme which uses the volume fraction field Φ of one phase that is advected by the flow to keep track of the position of the interface. The function Φ is unity in the region occupied entirely by one particular phase and zero in regions occupied fully by the other phase. As a consequence, the regions with fractional Φ contain the interface. The normal to the interface and surface tension effects are parameterized in terms of Φ and its gradients. Recent papers point to the growing interest in the problem of incorporating obstacles in flows.

Lai and Peskin [5] applied the IB method directly to the problem of flow past a cylinder, providing a formally second-order accurate numerical scheme. Fadlun et al. [6] proposed a second-order scheme for three-dimensional flows by using the IB principle where the body force is applied at the surface of the obstacle. In the same spirit but using other techniques, a volume force formulation was used by Xiao [7] for computing three-dimensional flows near suspended moving objects, while Bruneau et al. [8] simulated two-dimensional turbulence behind an array of cylinders.

In the present paper we describe an embedding method which combines features from both the IB and the VOF methods in order to compute flows past simple bodies. Like the IB method, the presence of the solid body is represented by an external body force density acting in the fluid equations. The determination of this force density is effected with the help of a volume

fraction field similar to the one defined in the VOF method. By restricting one's attention to rigid bodies, the volume fraction field Φ of the solid phase is fully determined by knowing the instantaneous position of the solid body. The computational domain (encompassing both the fluid and the body) is treated as a continuous fluid medium where the variables are computed in an Eulerian setting. In this context the fluid may be considered as made up of two pure phases, one being the rigid-body phase where the volume fraction is unity and the other the ordinary fluid phase where it is zero. In between, the medium is partially made up of fluid and solid phases and the variables vary continuously but steeply near this transition. The body force acts on the fluid to satisfy the condition that the velocity in the cells occupied by the solid should match the velocity of the rigid body. We validate the embedding method by solving the canonical problem of vortex shedding from a single stationary cylinder.We further restrict the current study to intermediate Reynolds numbers and quantify our results in terms of characteristic parameters of the global flow: the Strouhal number, and the lift and drag coefficients of the cylinder.

2 NUMERICAL METHOD

For simplicity, we consider the model problem of a viscous incompressible fluid in a two-dimensional square domain $\Omega = [0,1]\times[0,1]$. And the unsteady flow is governed by the momentum and continuity equations as following:

$$\frac{\partial \mathbf{u}}{\partial t} + \mathbf{u}\cdot\nabla\mathbf{u} + \nabla p = \frac{1}{Re}\Delta\mathbf{u}, \tag{1}$$

$$\nabla\cdot\mathbf{u} = 0. \tag{2}$$

Here $\mathbf{u}(\mathbf{x},t)=(u(\mathbf{x},t),v(\mathbf{x},t))$ and $p(\mathbf{x},t)$ are fluid velocity and fluid pressure, respectively. $\mathbf{x}=(x,y)$ is the coordinate, and Re is the Reynolds number. Hence we express the system to be an explicit form as

$$\frac{\partial u}{\partial t} + u\frac{\partial u}{\partial x} + v\frac{\partial u}{\partial y} + \frac{\partial p}{\partial x} = \frac{1}{Re}\left(\frac{\partial^2 u}{\partial x^2} + \frac{\partial^2 u}{\partial y^2}\right), \tag{3}$$

$$\frac{\partial v}{\partial t} + u\frac{\partial v}{\partial x} + v\frac{\partial v}{\partial y} + \frac{\partial p}{\partial y} = \frac{1}{Re}\left(\frac{\partial^2 v}{\partial x^2} + \frac{\partial^2 v}{\partial y^2}\right), \tag{4}$$

$$\frac{\partial u}{\partial x} + \frac{\partial v}{\partial y} = 0. \tag{5}$$

2.1 Staggered grid

Computational solutions of (3-5) are often obtained on a staggered grid. This implies that different dependent variables are evaluated at different grid points. The preferred staggered grid configuration is shown in Figure 1. It can be seen that pressures are defined at the center of each cell and that

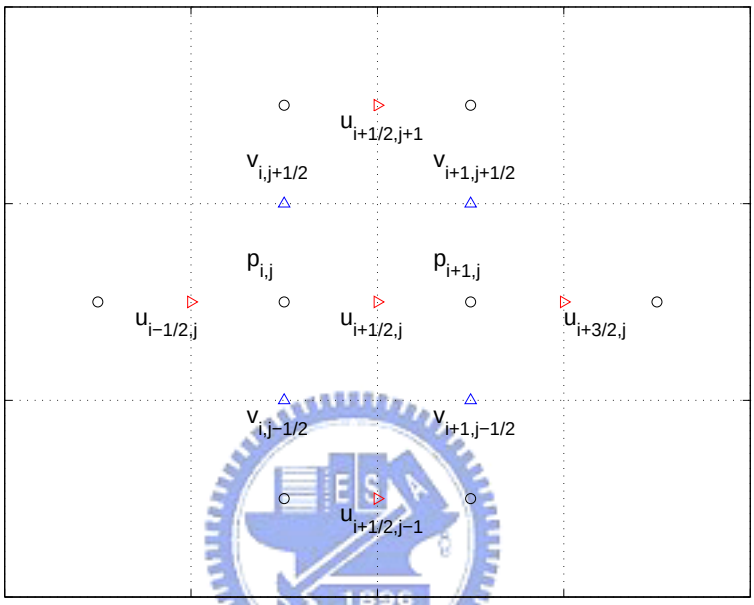

Figure 1: The staggered grid.

velocity components are defined at the center of the cell faces. Discretization of (2) on the staggered grid shown in Figure 1 gives

$$\frac{u_{i+1/2,j} - u_{i-1/2,j}}{\Delta x} + \frac{v_{i,j+1/2} - v_{i,j-1/2}}{\Delta y} = 0 \tag{6}$$

In addition a Taylor series expansion about the cell center indicates that they have a truncation error of $\boldsymbol{O}(\Delta x^2, \Delta y^2)$, even though only four grid points are involved.

The use of the staggered grid permits coupling of the u, v and p solutions at adjacent grid points. This in turn prevents the appearance of oscillatory solutions, particularly for p, that can occur if centered differences are used to discretize all derivatives on a non-staggered grid. The oscillatory solution is

a manifestation of two separate pressure solutions associated with alternate grid points, which the use of centered differences on a non-staggered grid permits. The oscillatory behavior is usually worse at high Reynolds number where the dissipative terms, which do introduce adjacent grid point coupling for u and v, are small. Clearly, from (3-5), there are no dissipative terms for p.

The use of staggered grids has some disadvantages. Computer programs based on staggered grids tend to be harder to interpret because it is desirable to associate a cluster of dependent variables with corresponding storage locations. Thus arrays storing u, v and p might associate storage location (i, j) with $u_{i+1/2,j}$, and $v_{i,j+1/2}$ and $p_{i,j}$ as Figure 1. Generally boundary conditions are more difficult to impose consistently with a staggered grid, since at least one dependent variable, u or v, will not be defined on a particular boundary. If the grid is non-rectangular, and generalized coordinates are used, the incorporation of a staggered grid is more complicated.

In discretizing (3-5) the following finite difference expressions are used:

$$\begin{aligned}
\left[\frac{\partial u}{\partial t}\right]_{i+1/2,j} &= \frac{u^{n+1}_{i+1/2,j} - u^{n}_{i+1/2,j}}{\Delta t} + \boldsymbol{O}(\Delta t), \\
\left[\frac{\partial u}{\partial x}\right]_{i+1/2,j} &= \frac{u_{i+3/2,j} - u_{i-1/2,j}}{2\Delta x} + \boldsymbol{O}(\Delta x^2), \\
\left[\frac{\partial u}{\partial y}\right]_{i+1/2,j} &= \frac{u_{i+1/2,j+1} - u_{i+1/2,j-1}}{2\Delta y} + \boldsymbol{O}(\Delta y^2), \\
\left[\frac{\partial^2 u}{\partial x^2}\right]_{i+1/2,j} &= \frac{u_{i+3/2,j} - 2u_{i+1/2,j} + u_{i-1/2,j}}{\Delta x^2} + \boldsymbol{O}(\Delta x^2), \\
\left[\frac{\partial^2 u}{\partial y^2}\right]_{i+1/2,j} &= \frac{u_{i+1/2,j+1} - 2u_{i+1/2,j} + u_{i+1/2,j-1}}{\Delta y^2} + \boldsymbol{O}(\Delta y^2).
\end{aligned} \tag{7}$$

In the above expression terms like $v_{i+1/2,j}$ appear, which are not defined in Figure 1. To evaluate such terms, linear interpolation is employed, that is,

$$[v]_{i+1/2,j} = 0.25(v_{i,j-1/2} + v_{i+1,j-1/2} + v_{i,j+1/2} + v_{i+1,j+1/2}) \tag{8}$$

Similarly, $u_{i,j+1/2}$ is evaluated as

$$[u]_{i,j+1/2} = 0.25(u_{i-1/2,j} + u_{i-1/2,j+1} + u_{i+1/2,j} + u_{i+1/2,j+1}) \tag{9}$$

2.2 MAC formulation

One of the earliest, and most widely used, methods for solving (3-5) is the Marker and Cell (MAC) method [10] due to Amsden and Harlow (1970). The method is characterized by the use of a staggered grid and the solution of a Poisson equation for the pressure at every time-step. Although the original form of the MAC method has certain weakness, the use of a staggered grid and a Poisson equation for the pressure has been retained in many modern methods derived from the MAC method.

In the MAC formulation the discretizations (7) allow the following explicit algorithm to be generated from (3 and 4):

$$u_{i+1/2,j}^{n+1} = F_{i+1/2,j}^{n} - \frac{\Delta t}{\Delta x}(p_{i+1,j}^{n+1} - p_{i,j}^{n+1}), \tag{10}$$

where

$$\begin{aligned} F_{i+1/2,j}^{n} &= u_{i+1/2,j}^{n} + \Delta t[\frac{u_{i+3/2,j} - 2u_{i+1/2,j} - u_{i-1/2,j}}{Re\Delta x^2} \\ &+ \frac{u_{i+1/2,j+1} - 2u_{i+1/2,j} - u_{i+1/2,j-1}}{Re\Delta y^2} \\ &- u_{i+1/2,j}\frac{u_{i+3/2,j} - u_{i-1/2,j}}{\Delta x} \\ &- v_{i+1/2,j}\frac{u_{i+1/2,j+1} - u_{i+1/2,j-1}}{\Delta y}]^n. \end{aligned} \tag{11}$$

Similarly the discretized form of (4) is written as

$$v_{i,j+1/2}^{n+1} = G_{i,j+1/2}^{n} - \frac{\Delta t}{\Delta y}(p_{i,j+1}^{n+1} - p_{i,j}^{n+1}), \tag{12}$$

where

$$\begin{aligned} G_{i,j+1/2}^{n} &= v_{i,j+1/2}^{n} + \Delta t[\frac{u_{i+1,j+1/2} - 2v_{i,j+1/2} - v_{i-1,j+1/2}}{Re\Delta x^2} \\ &+ \frac{v_{i,j+3/2} - 2v_{i,j+1/2} - v_{i,j-1/2}}{Re\Delta y^2} \\ &- u_{i,j+1/2}\frac{v_{i+1,j+1/2} - v_{i-1,j+1/2}}{\Delta x} \\ &- v_{i,j+1/2}\frac{v_{i,j+3/2} - v_{i,j-1/2}}{\Delta y}]^n. \end{aligned} \tag{13}$$

In (10 and 12) p appears implicitly; however, p^{n+1} is obtained before (10 and 12) are used, as follows. The continuity equation is discretized as

$$\frac{u^{n+1}_{i+1/2,j} - u^{n+1}_{i-1/2,j}}{\Delta x} + \frac{v^{n+1}_{i,j+1/2} - v^{n+1}_{i,j-1/2}}{\Delta y} = 0 \tag{14}$$

Substituting right-hand-side of (10 and 12) into (15), we rewrite (15) as a discrete Poisson equation for the pressure

$$\begin{aligned}\left[\frac{p_{i+1,j} - 2p_{i,j} - p_{i-1,j}}{\Delta x^2} + \frac{p_{i,j+1} - 2p_{i,j} - p_{i,j-1}}{\Delta y^2}\right]^{n+1} \\ = \frac{1}{\Delta t}\left[\frac{F^n_{i+1/2,j} - F^n_{i-1/2,j}}{\Delta x} + \frac{G^n_{i,j+1/2} - G^n_{i,j-1/2}}{\Delta y}\right]\end{aligned} \tag{15}$$

The equation is solved at every time-step using direct Poisson solver, and the solution p^{n+1} will be substituting into (10 and 12) to obtain u^{n+1} and u^{n+1}.

2.3 Projection method

First, we introduce a first-order projection method to complete our preliminary for solving the Navier-Stokes equation. The general procedure for a projection method is a predictor-corrector approach. In the first step an intermediate velocity field denoted by $\mathbf{u}^*$ is computed utilizing the momentum equations. This velocity does not satisfy the continuity equation. In the second step a Poisson equation for the pressure which is derived from the continuity equation is solved. In the last step $\mathbf{u}^*$ is projected onto a divergence-free velocity field by the computed pressure. The three step are now described in more detail for our treatment problem.

Step1: This is a prediction step for $\mathbf{u}^*$.

$$\mathbf{u}^* = \mathbf{F}^n \tag{16}$$

The components of $\mathbf{F} = (F, G)$ are expressed in (11 and 13).

Step2: Solve a Poisson equation for pressure by using the direct Poisson solver.

$$\Delta p^{n+1} = \frac{1}{\Delta t}\nabla \cdot \mathbf{u}^*. \tag{17}$$

Step3: The projection step.

$$\mathbf{u}^{n+1} = \mathbf{u}^* - \Delta t \nabla p^{n+1}. \tag{18}$$

Note that this procedure has second-order accuracy in space and first-order accuracy in time. Since the corresponding algorithms for u^{n+1} and v^{n+1} are explicit, there is a restriction on the maximum time-step for a stable solution [11].

$$\begin{aligned} &0.25(\mid u \mid + \mid v \mid)^2 \Delta t Re \leq 1 \quad \text{and} \\ &\Delta t/(Re\Delta x^2) \leq 0.25, \quad \text{assuming that} \quad \Delta x^2 = \Delta y^2 \end{aligned} \tag{19}$$

In order to improve the restriction on the maximum time step and reduce the error from the time discretization, we introduce a second-order projection method to momentum and continuity equations. The detailed procedures are described as the following steps.

Step1: This is a prediction step to evaluate the intermediate velocity field $\mathbf{u}^*$ by the Helmholtz-type solver.

$$\frac{3\mathbf{u}^* - 4\mathbf{u}^n + \mathbf{u}^{n-1}}{2\Delta t} + 2(\mathbf{u}^n \cdot \nabla)\mathbf{u}^n - (\mathbf{u}^{n-1} \cdot \nabla)\mathbf{u}^{n-1} + \nabla p^n = \frac{1}{Re}\Delta \mathbf{u}^* \tag{20}$$

In this step the unknown $\mathbf{u}^*$ is treated implicitly, so we can relax the restriction of maximum time-step. Moreover, this algorithm is second-order accurate in time.

Step2: By the Hodge decomposition there exist a potential function ϕ and a divergence-free velocity field $\mathbf{u}^{n+1}$ such that

$$\mathbf{u}^* = \mathbf{u}^{n+1} + \frac{2\Delta t}{3}\Delta \phi^{n+1} \tag{21}$$

Now taking the divergence operator into (21) and using the divergence-free property, we have

$$\Delta \phi^{n+1} = \frac{3}{2\Delta t}\nabla \cdot \mathbf{u}^* \tag{22}$$

Furthermore, a Poisson solver is used again to obtain ϕ^{n+1}.

Step3: Project $\mathbf{u}^*$ onto $\mathbf{u}^{n+1}$ as

$$\mathbf{u}^{n+1} = \mathbf{u}^* - \frac{2\Delta t}{3}\Delta\phi^{n+1}. \tag{23}$$

and ∇p^{n+1} can be obtained as

$$\nabla p^{n+1} = \nabla p^n + \nabla\phi^{n+1} - \frac{1}{Re}\Delta\mathbf{u}^*. \tag{24}$$

2.4 Combination of projection method and VOF approach

The case of two immiscible fluid phases separated by an involving interface has been treated by the VOF method, developed by Hirt and Nichols [3]. In this section, we shall describe how to combine the VOF and projection methods to simulate the flow through a solid object. For simplicity, we consider a cell occupied by fluid and solid as Figure 2. We first define a volume fraction field $\Phi_{i,j}$ on the cell center as

$$\Phi_{i,j} = \frac{vol(object)}{vol(cell)} \tag{25}$$

where $vol(cell)$ is the area of cell (i,j) and $vol(object)$ is the area of the object inside cell (i,j). Note that the volume-fraction field Φ is only defined on cell center.

The embedding method refers to a scheme for computing flows in the vicinity of stationary or moving solid bodies using the space-filling Cartesian grid which passes through the solid bodies as well. The governing equations for the fluid flow (i.e., the Navier-Stokes and continuity equations) are solved everywhere, including the cells which are occupied by the solid body. The presence of the solid body is accounted for, however, by adding a force field to the fluid momentum equation in those cells which are fully or partially occupied by the solid phase. The magnitude and direction of this body force density is determined at every time step of the computation by the requiring the value of the velocity in those cells to match the prescribed velocity of the solid body. This is done with the aid of a volume-fraction field which determines what fraction of each computational cell in the Cartesian grid is occupied by the solid phase. In cells where the solid volume fraction is unity,

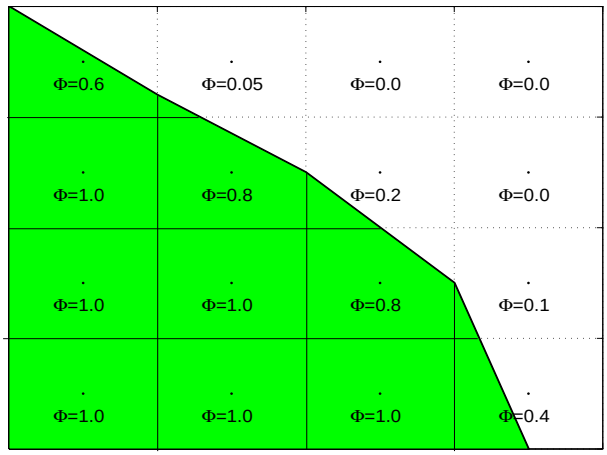

Figure 2: The figure of the volume fraction field.

the velocity is set exactly equal to that of the body, and in those where the volume fraction is between zero and one, the velocity is only adjusted partially, in proportion to the volume fraction. Cells which which are free from the solid and have a volume fraction of zero do not posses this body-force and are not affected in that step of the computation.

More specifically, consider unsteady flow of an incompressible fluid governed by the continuity and the Navier-Stokes equations:

$$\frac{\partial \mathbf{u}}{\partial t} + \mathbf{u} \cdot \nabla \mathbf{u} + \nabla p = \frac{1}{Re} \Delta \mathbf{u} + \mathbf{f}, \tag{26}$$

$$\nabla \cdot \mathbf{u} = 0. \tag{27}$$

In the current implementation of the embedding method, our treatment system has been solved on a staggered grid. In the staggered grid, within cell (i, j), the pressure and volume fraction field are assigned to the cell center, while the horizontal and vertical velocity components are respectively assigned to the face center of the right and top edges of the cell. The time integration is performed by the operator splitting technique in three distinct steps. The three fractional steps for time-evolution of the primitive variables (velocity and pressure) are now described in more detail for the specific case of two-dimensional flow past a single stationary cylinder for which the method has been validated.

Step1: This prediction step treats only the advection, diffusion and pressure parts to obtain the first intermediate velocity field $\mathbf{u}^*$. Here the velocity field is determined in the entire computational domain regardless of the position of the immersed body. Our current implementation of this step is implicit, hence the stability consideration is relaxed. And use the Helmholtz-type solver to march the solution

$$\frac{3\mathbf{u}^* - 4\mathbf{u}^n + \mathbf{u}^{n-1}}{2\Delta t} + 2(\mathbf{u}^n \cdot \nabla)\mathbf{u}^n - (\mathbf{u}^{n-1} \cdot \nabla)\mathbf{u}^{n-1} + \nabla p^n = \frac{1}{Re}\Delta \mathbf{u}^*. \quad (28)$$

Step2: The second step is a modified step, which contains the essential component of the embedding method, allows us to take into account the presence of the cylinder. At this stage, one treats the system as a "binary" fluid. One phase is simply the ordinary outside the rigid body while the other is the cylinder phase itself, within which the velocity is expected to vanish. To identify exactly the cells assigned to each phase, a volume-fraction field is defined as the fraction of the area of each cell occupied by the cylinder. By imposing the body force term $\mathbf{f}$ in those cells that are partially or fully occupied by the cylinder, we modify the velocity field to make it vanish in the cylinder. Namely, the presence of the body force implies the update velocity:

$$\mathbf{u}^{**} = \mathbf{u}^* + \frac{2\Delta t}{3}\mathbf{f} \quad (29)$$

where $\mathbf{u}^{**}$ is the second intermediate velocity field. The embedding method determines the force $\mathbf{f}$ to make the updated velocity $\mathbf{u}^{**}$ vanish within the cylinder. For this purpose and to define exactly which cells are involved in the modification of the velocity, the volume-fraction field Φ of the cylinder phase is computed in the entire mesh. For the cells located strictly inside the cylinder, the volume fraction is unity. It decreases in the vicinity of the cylinder boundary, which represents the transition region between the two phases, to a value of zero in the region of the computational domain entirely within the fluid. With respect to the staggered grid, the volume fraction function is a cell-centered quantity. However, in this formulation, $p(i,j)$, $u(i+1/2,j)$, and $v(i,j+1/2)$ are respectively assigned to the center, right edge and top edge of the square cell (i,j). In order to represent accurately the presence of the cylinder at the nodes where the velocity components u and v are defined, two similar functions $\Phi^x_{i+1/2,j}$ and $\Phi^y_{i,j+1/2}$ are introduced.

$$\begin{cases} \Phi^x_{i+1/2,j} = 0.5(\Phi_{i,j} + \Phi_{i+1,j}) & \text{if point } (i+1/2, j) \text{ outside the object,} \\ \Phi^x_{i+1/2,j} = 1.0 & \text{if point } (i+1/2, j) \text{ inside the object,} \\ \Phi^y_{i,j+1/2} = 0.5(\Phi_{i,j} + \Phi_{i,j+1}) & \text{if point } (i, j+1/2) \text{ outside the object,} \\ \Phi^y_{i,j+1/2} = 1.0 & \text{if point } (i, j+1/2) \text{ inside the object.} \end{cases}$$

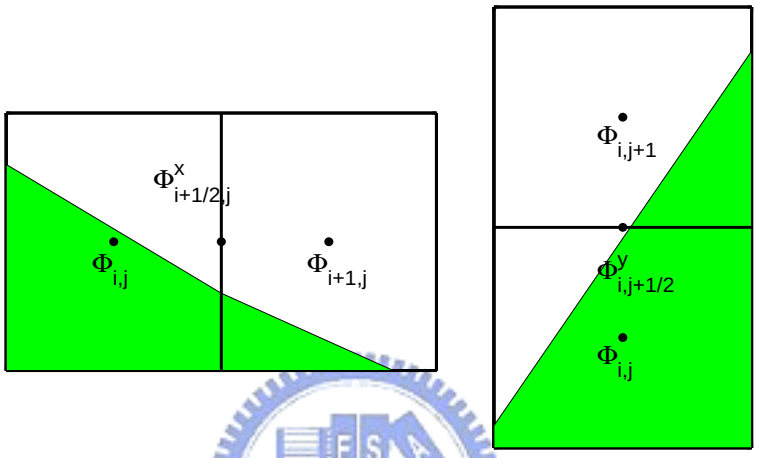

Figure 3: The figure of Φ^x and Φ^y.

To make the velocity vanish inside the cylinder but remain unchanged in the fluid, in the case of the velocity component u, we set

$$u^{**}_{i+1/2,j} = (1 - \Phi^x_{i+1/2,j}) u^*_{i+1/2,j} \tag{30}$$

Thus, in cells (i, j) inside the cylinder, the velocity along the x-direction is vanished. In the boundary cells, the updated velocity is partially modified since Φ^x is between zero and one. Finally, outside the cylinder u^{**} is identical to u^* so that the flow remains unchanged. By replacing the required velocity (30) into (29), the value of the body force is deduced:

$$(f_x)_{i+1/2,j} = \frac{-3\Phi^x_{i+1/2,j} u^*_{i+1/2,j}}{2\Delta t} \tag{31}$$

The force component f_x is applied at the same collocation point in cell (i, j) where u is defined. The force component $(f_y)_{i,j+1/2}$ can be defined similarly.

Step3: By the Hodge decomposition there exists a potential function ϕ and a divergence-free velocity field $\mathbf{u}^{n+1}$such that

$$\mathbf{u}^{**} = \mathbf{u}^{n+1} + \frac{2\Delta t}{3}\Delta\phi^{n+1} \tag{32}$$

Now taking the divergence operator into the above equation and using the divergence-free property, we have

$$\Delta\phi^{n+1} = \frac{3}{2\Delta t}\nabla \cdot \mathbf{u}^{**} \tag{33}$$

Furthermore, the Poisson solver is used again to obtain ϕ^{n+1}.

Step4: The last fractional step is the projection step as

$$\mathbf{u}^{n+1} = \mathbf{u}^{**} - \frac{2\Delta t}{3}\nabla\phi^{*}, \tag{34}$$

and the pressure can be obtained.

$$p^{n+1} = p^{n} + \phi^{n+1} - \frac{1}{Re}(\nabla \cdot \mathbf{u}^{**}) \tag{35}$$

3 Numerical simulations

3.1 Accuracy check

In this section, we will check our Navier-Stokes solver is second-order accurate in both time and space. The following two-dimensional unsteady flow which is a solution to the Navier-Stokes equations on $\Omega = [0,1] \times [0,1]$. We compute this problem in different mesh size and list the maximum norm of errors of the velocity and pressure in Table 1.

$$\begin{aligned} u(x,y,t) &= -\cos(\pi x)\sin(\pi y)\exp^{-2\pi^2 t/Re} \\ v(x,y,t) &= \sin(\pi x)\cos(\pi y)\exp^{-2\pi^2 t/Re} \\ p(x,y,t) &= -0.25(\cos(2\pi x) + \cos(2\pi y))\exp^{-4\pi^2 t/Re} \end{aligned} \tag{36}$$

The maximum error at $T = 10$						
Grid	u	order	v	order	p	order
10×10	6.1204e-005	-	6.0240e-005	-	4.4999e-004	-
20×20	1.4524e-005	2.08	1.4435e-005	2.06	1.1631e-004	1.95
40×40	3.5976e-006	2.01	3.6321e-006	1.99	2.9128e-005	2.00
80×80	9.0365e-007	1.99	9.1327e-007	1.99	7.2424e-006	2.01

Table 1: The maximum norm of error of different quantities with $Re = 100$.

3.2 Flow in a driven cavity

Figure 4 shows the geometry and the boundary conditions for the flow in a driven cavity. Flow is driven by the upper wall, and several standing vortices exist inside the cavity whose characteristics are functions of Reynolds numbers [12]. Our computational domain is still $\Omega = [0, 1] \times [0, 1]$ and the result is shown in Figure 5.

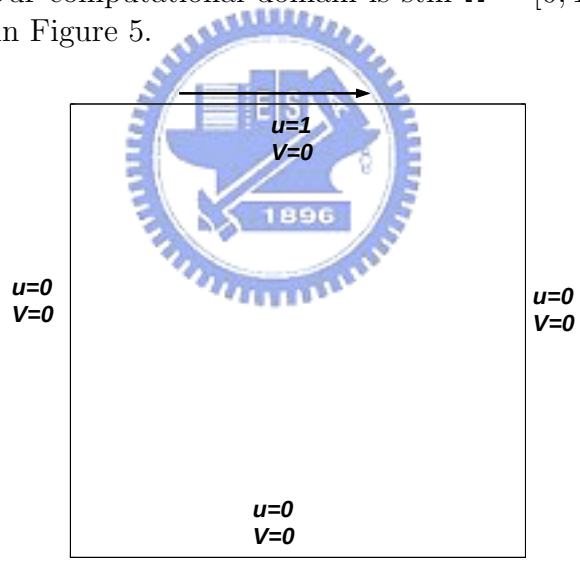

Figure 4: The geometry and boundary conditions for a driven cavity.

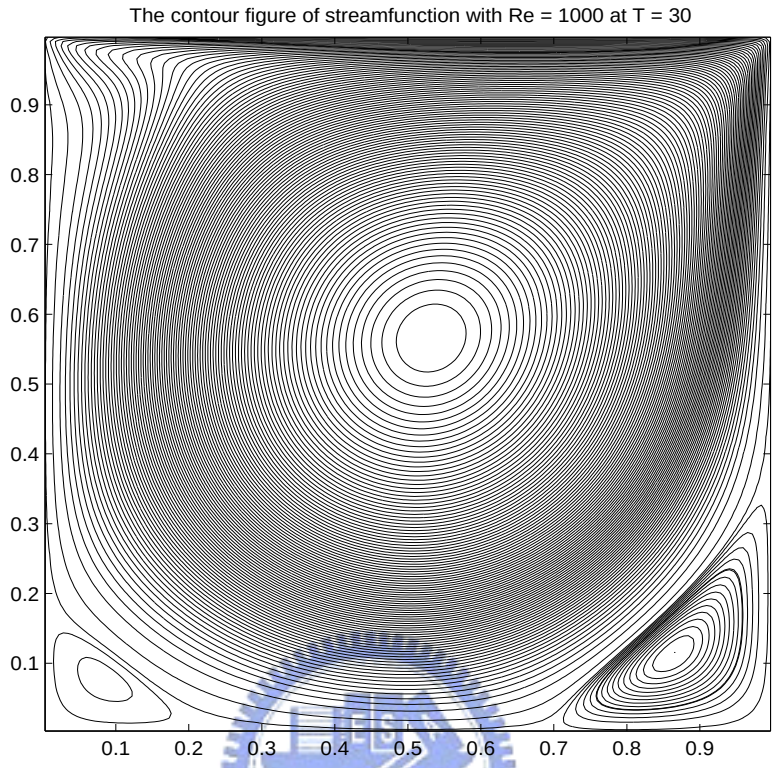

Figure 5: A contour figure of a driven cavity at $T = 30.0$ with $Re = 1000$, $\Delta x = 1/160$, and $\Delta t = 1/400$.

3.3 A cylinder in the driven cavity

In this subsection, we add a rigid body into the driven cavity as Figure 6, which shows the geometry and the boundary conditions for the flow in a driven cavity. Flow is driven by the upper wall, and several standing vortices exist inside the cavity like the last example except for the primary vortex moving to the right-top corner [13]. Our computational domain is the same as the last example and several results are expressed as the followings:

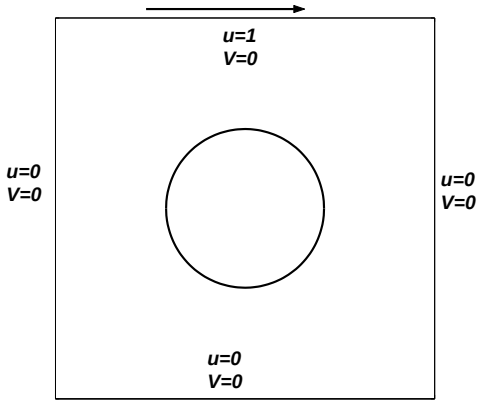

Figure 6: The geometry and boundary conditions for a driven cavity with a circular cylinder.

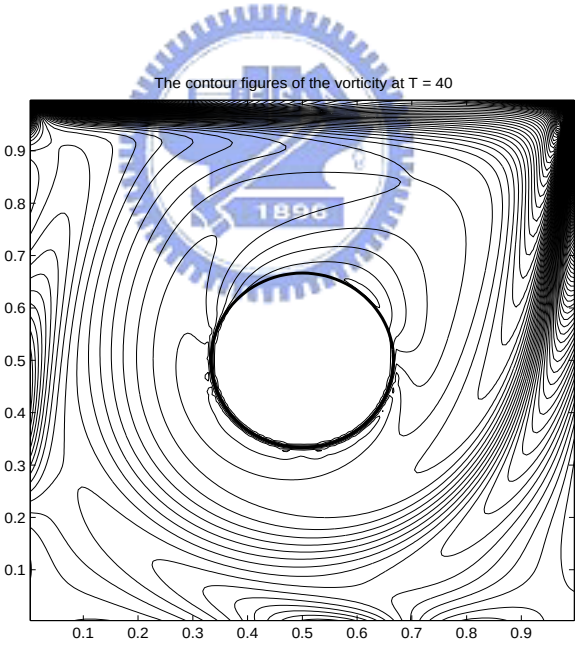

Figure 7: Figure of vorticity at $T = 30.0$ with $\Delta x = 1/160$, $\Delta t = 1/400$, and $Re = 1000$.

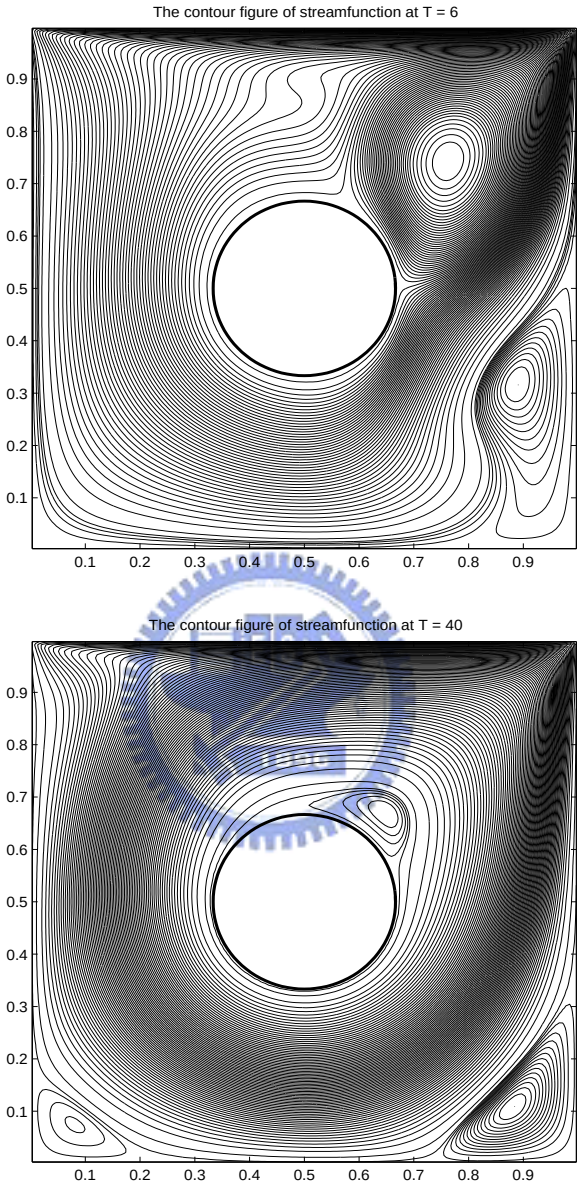

Figure 8: Figures of stream function at $T = 6.0$ and $T = 40.0$, respectively.

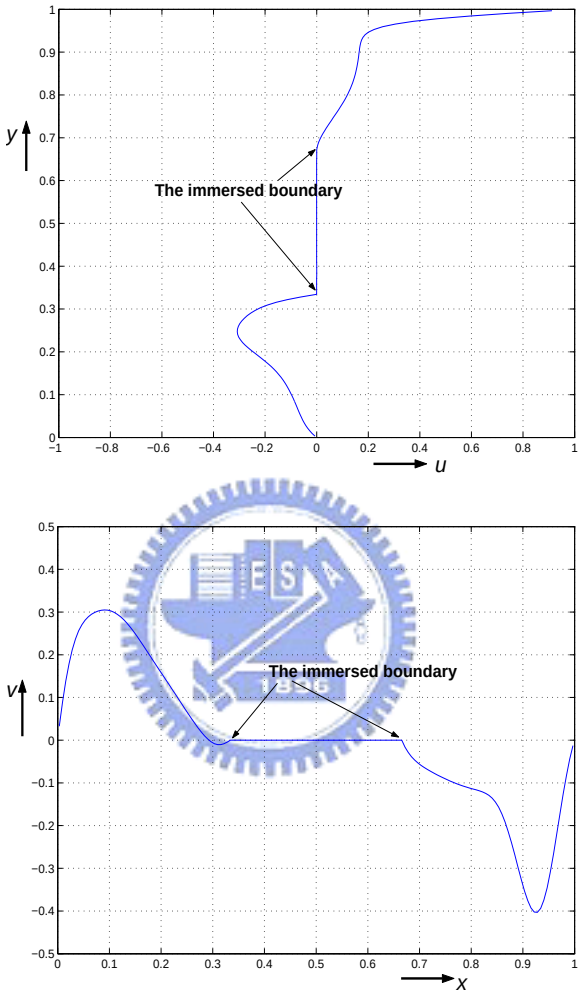

Figure 9: Figures of velocities u and v on $x = 0.5$ and $y = 0.5$ at $T = 12$, respectively.

3.4 The flow around a cylinder

The flow around a circular cylinder immersed in the fluid stream is studied as a typical model problem for separated flows and boundary layer theory. It has been the subject of many theoretical, experimental and computational works. Depending on the Reynolds number, different kind of flow behaviors can be characterized. At a lower Reynolds number, the flow is viscosity dominated and is called the creeping flow. At somewhat higher Reynolds number (up to $Re = 40$), two symmetrical standing vortices are formed and attached behind the cylinder. When the Reynolds number gets higher, these vortices can stretch farther and farther downstream from the cylinder and eventually become distorted break apart to develop an alternating vortex shedding called the Kármán vortex street. For Reynolds number up to 200, this flow is purely laminar and the vortex street is stable and time periodic. Readers who are interested in more detail about this flow can refer to [3].

Drag coefficient: The drag force on a body submerged in a stream arises from two sources, the shear stress and the pressure distribution along the body. The dimensionless drag coefficient is defined by

$$C_D = -\frac{2}{\rho u_\infty^2 D} \int_\Gamma f_x dA. \tag{37}$$

where f_x is the drag force, u_∞ is the free-stream velocity, ρ is the density of the fluid and D is the diameter of the object. In the present computation, we have the opportunity to evaluate the drag force.

Lift coefficient: When the body starts shedding a vortex, a lift force on the body is generated by the fluid. The dimensionless lift coefficient is defined by

$$C_L = -\frac{2}{\rho u_\infty^2 D} \int_\Gamma f_y dA. \tag{38}$$

where f_y is the lift force.

Strouhal number: When the steady flow becomes unstable and the body starts shedding vortices, the frequency with which the vortices are shed from the body can be made dimensionless by formula

$$S_t = \frac{f_q}{u_\infty D}. \tag{39}$$

where f_q is the vortex shedding frequency. The new parameter S_t is called the Strouhal number. In our computation, it is easy to measure the dimensionless time period T_p between vortices shedding. Thus, using the fact that $f_q = 1/T_p$ and hence S_t is measured by

$$S_t = \frac{2}{T_p}. \tag{40}$$

Related computational results: In all cases, we choose a large computational domain as Figure 10 and a cylinder with diameter $D = 1.0$ inside the domain. The fluid density is 1.0 and the far field velocity u_∞ is 1.0. The mesh size are $\Delta x = 0.1$ and $\Delta t = 0.02$. In Table 2 We choose $\Delta x = 0.05$ and $\Delta t = 0.01$, and show the comparison of different quantities with other authors. The simulations of the streamfunction and the vorticity of different Reynolds number are shown in figures behind Table 2.

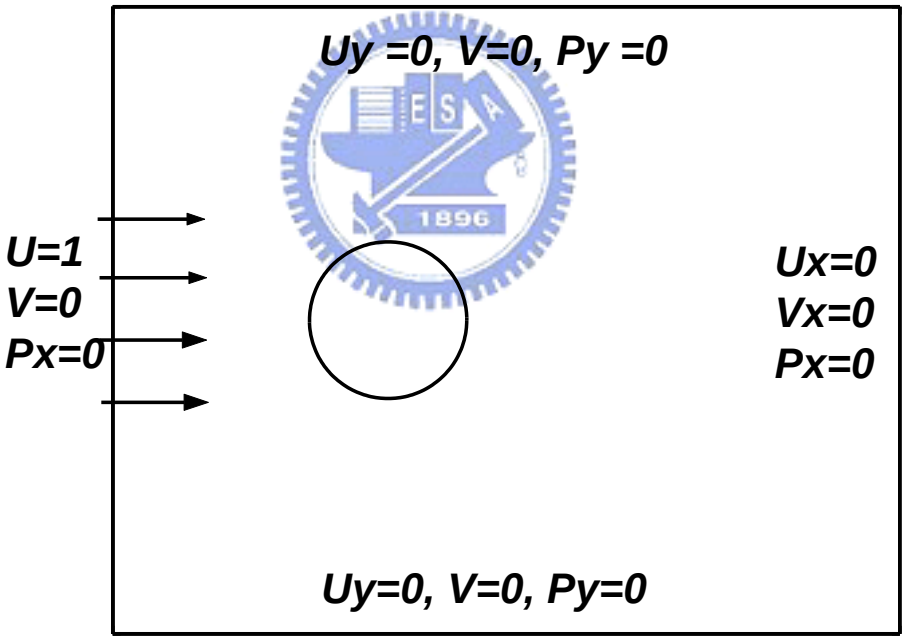

Figure 10: The geometry and boundary conditions for the flow around a circular cylinder.

The comparison of drag coefficients for different Reynolds numbers						
Re	present	Lai & Peskin	Kim et al.	Silva et al.	Ye et al.	Tritton (exp.)
20	2.18	-	-	2.04	2.03	2.22
40	1.64	-	1.51	1.54	1.52	1.48
80	1.41	-	-	1.40	1.37	1.29
100	1.38	1.44	1.33	1.39	-	-
150	1.36	1.44	-	1.37	-	-

The comparison of lift coefficient for different Reynolds numbers			
Re	present	Lai & Peskin	Kim et al.
80	0.18	-	-
100	0.30	0.33	0.32
150	0.37	-	-

The comparison of Strouhal number for different Reynolds numbers					
Re	present	Lai & Peskin	Silva et al.	Ye et al.	Williamson (exp.)
80	0.157	-	0.15	0.15	0.150
100	0.169	0.165	0.16	-	0.166
150	0.186	0.184	0.18	-	0.183

Table 2: The comparison of different quantities.

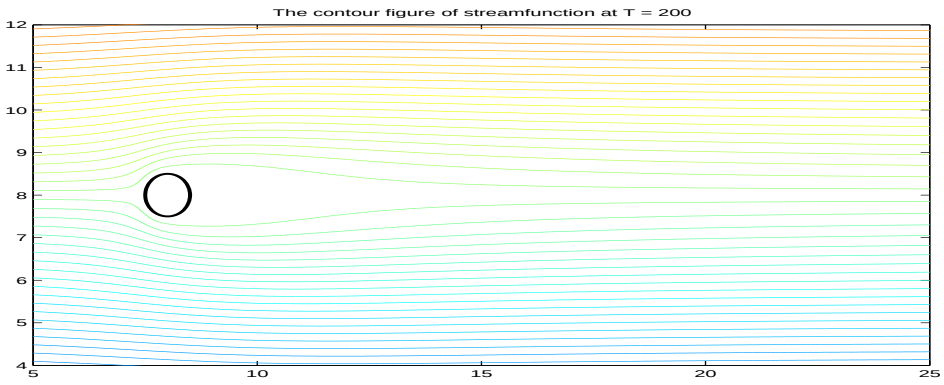

Figure 11: The contour figure of streamfunction at $Re = 40$.

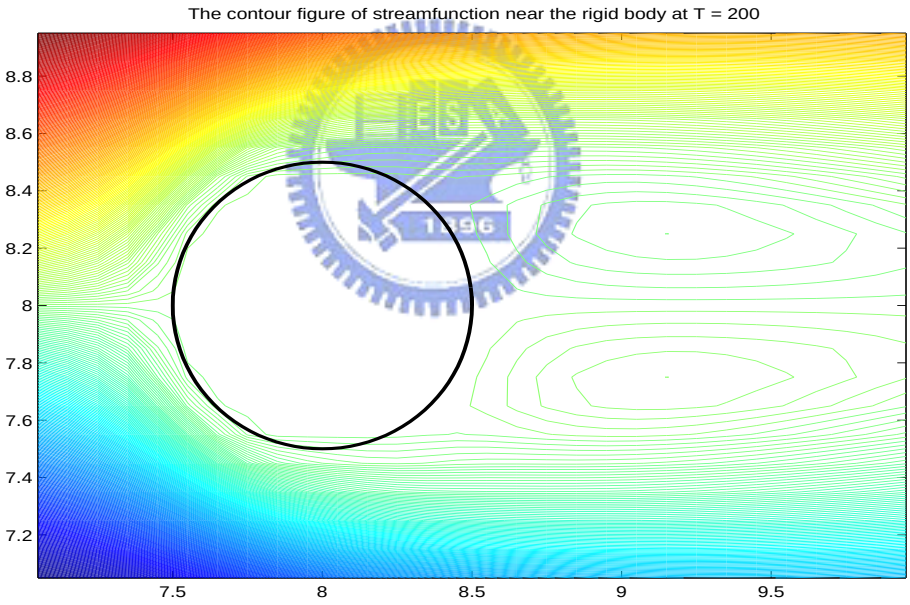

Figure 12: The contour figure near the rigid body.

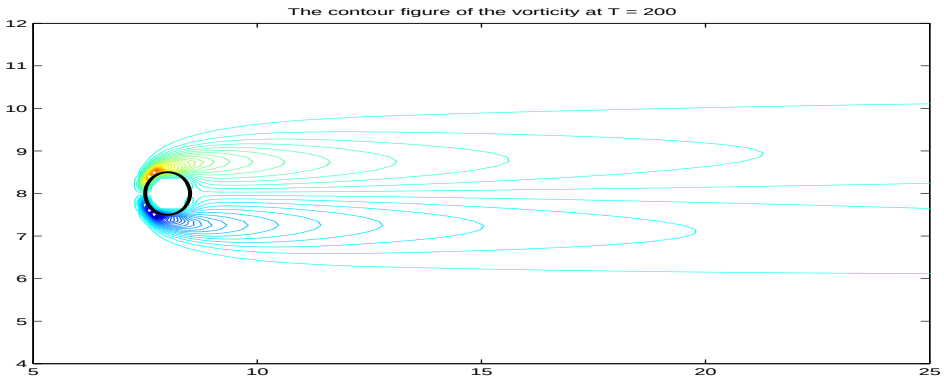

Figure 13: The contour figure of vorticity at $Re = 40$.

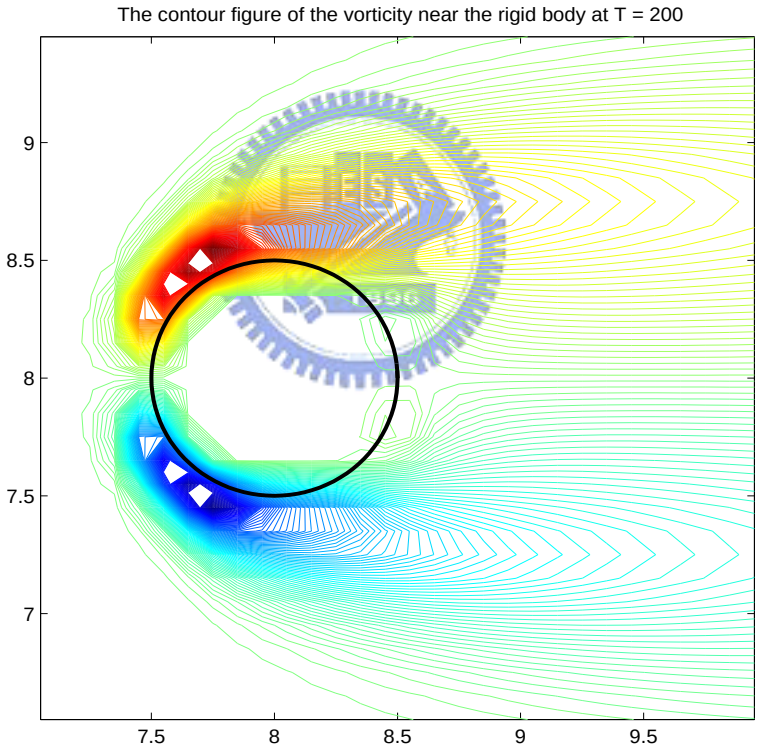

Figure 14: The contour figure near the rigid body.

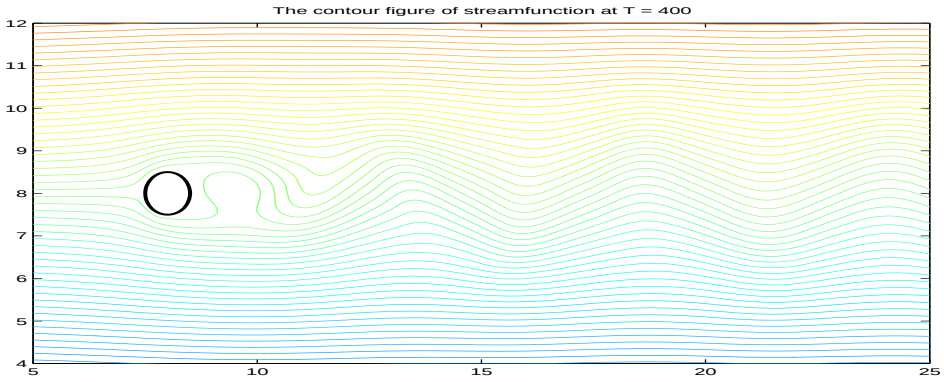

Figure 15: The contour figure of streamfunction at $Re = 100$.

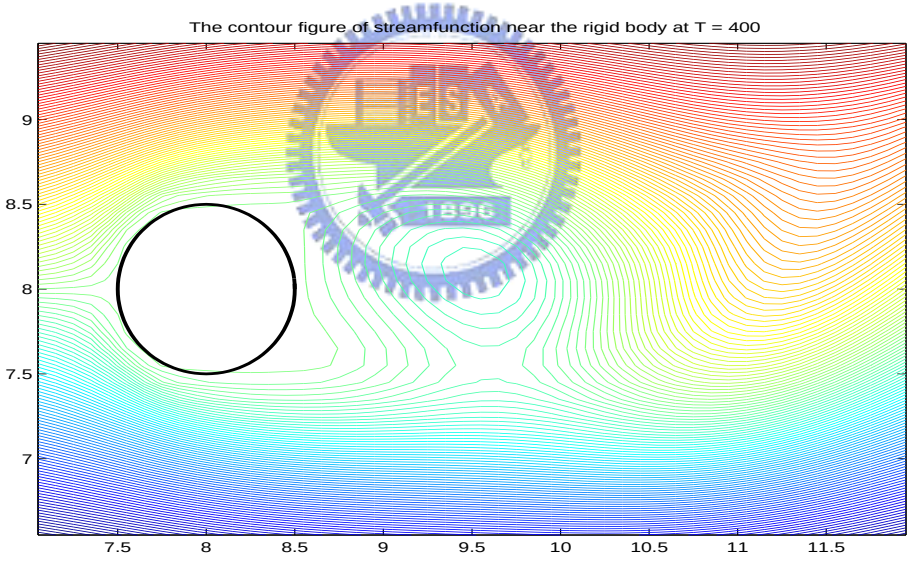

Figure 16: The contour near the rigid body.

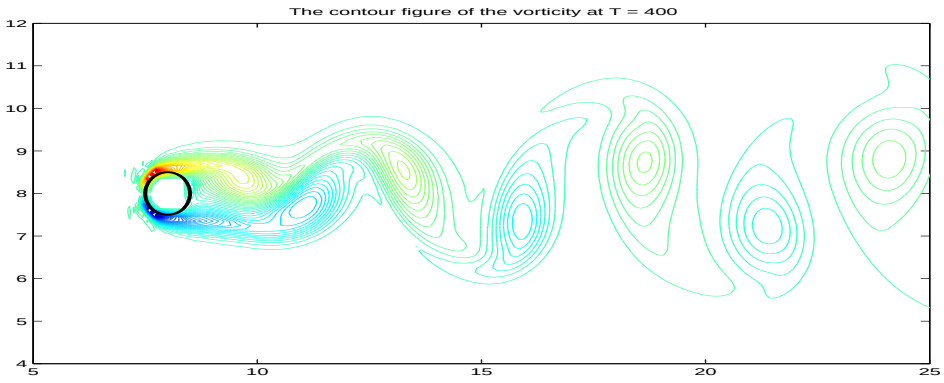

Figure 17: The contour figure of vorticity at $Re = 100$.

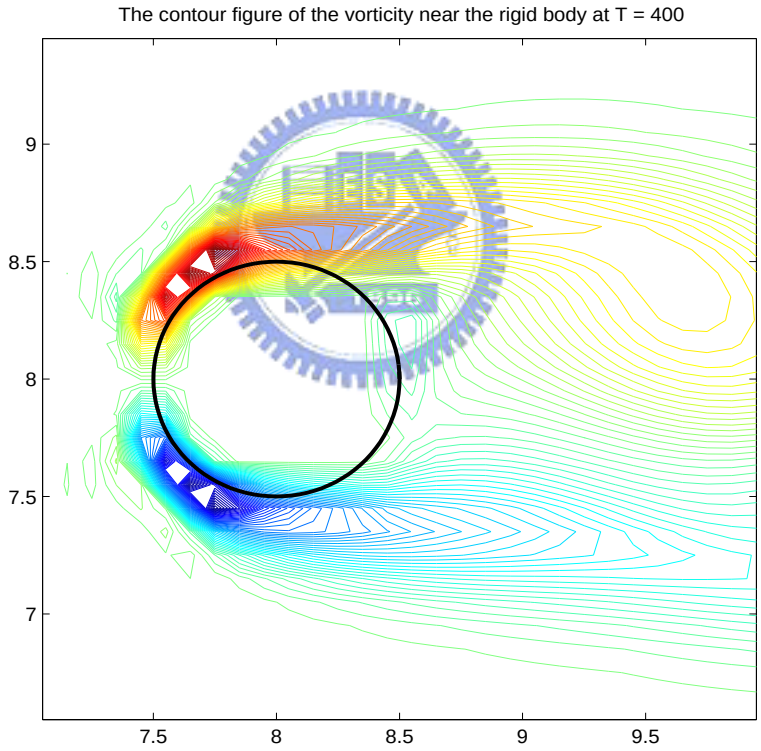

Figure 18: The contour near the rigid body.

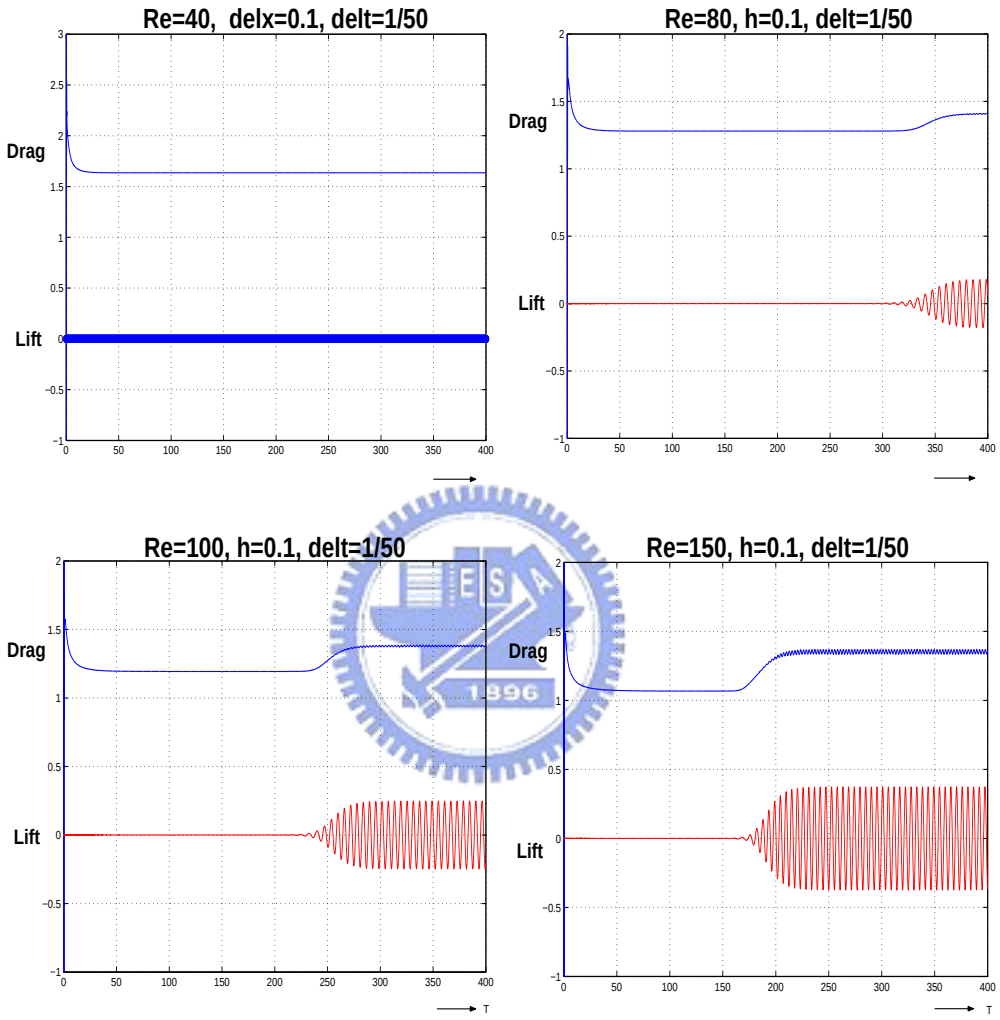

Figure 19: The time evolution of drags and lifts at different Reynolds numbers.

4 Conclusion

In this thesis, we develop a simple second-order scheme to simulate the flow around a solid body. The method treats the fluid-solid as a binary fluid where the volume of fluid is introduced. The fluid equations are solved by a implicit version of the projection method where the velocity is modified in the intermediate step by the presence of the solid body. This method is validated by the simulation of fluid around a stationary solid body and the physical quantities, for instance, the lift and drag coefficients, and the Strouhal number, are very close to those quantities from experiments. The application of this method to more general flow problem such as moving object flow is under way.

References

[1] Peskin, C.S. (1977). Numerical analysis of blood flow in the heart. J. Comput. Phys., 25, 220–252. Mc Queen, D.M., and Peskin, C.S. (1989). A 3-dimensional computational method for blood-flow in the heart. 1. Immersed elastic fibers in a viscous incompressible fluid J. Comput. Phys., 81(2), 372–405.

[2] Gueyffier, D., Lie, J., Nadim, A., Scardovelli, R., and Zaleski, S. (1999). Volume-of-fluid interface tracking with smoothed surface stress methods for three-dimensional flows. J. Comp. Phys., 152, 423–456.

[3] Hirt, C.W., and Nichols, B.W. (1981). Volume of fluid (VOF) method for dynamics of free boundaries. J. Comput. Phys., 39, 201–225.

[4] Scardovelli, R., and Zaleski, S. (1999). Direct numerical simulation of free-surface and interfacial flows. Ann. Rev. Fluid Mech., 31, 567–603.

[5] Lai, M.C., and Peskin, C.S. (2000). An immersed boundary method with formal second-order accuracy and reduced numerical viscosity. J. Comput. Phys., 160(2), 705–719.

[6] Fadlun, E.A., Verzicco, R., Orlandi, P., and Mohd-Yusof, J. (2000). Combined immersed boundary finite-difference methods for three-dimensional complex simulations. J. Comput. Phys., 161(2), 35–60.

[7] Xiao, F. (1999). A computational model for suspended large rigid bodies in 3D unsteady viscous flows. J. Comput. Phys., 155(2), 348–379.

[8] Bruneau, C.H., Greffier, O., and Kellay, H. (1999). Numerical study of grid turbulence in two dimensions and comparisons with experiments on turbulent soap films. Physica Rev. E, Part A60(2), R1162–1165.

[9] J.F. Ravoux, A. Nadim, and H. Haj-Hariri, (2003). An Embedding Method for Bluff Body Flows: Interactions of Two Side-by-Side Cylinder Wakes. Theoret. Comput. Fluid Dynamics 16:433–466.

[10] C.A.J. Fletcher. Computational Techniques for Fluid Dynamics, (1991).

[11] P. Roger, T. Thomas. Computational methods for fluid flow, p. 148, (1983).

[12] J. Kim, and P. Moin, (1985). Application of a fraction-step method to incompressible Navier-Stokes equations. J. Comput. Phys., 59, 308–323.

[13] Dartzi Pan, An implicit pressure correction method for incompressible flows with immersed bodies. (From Institute of Aeronautics, National Cheng Kung University, Taiwan).